Identification of Dy^{3+}/Dy^{2+} as Electron Trap in Persistent Phosphors

Jonas J. Joos,[1,2,*] Katleen Korthout,[1,2] Lucia Amidani,[3,†] Pieter Glatzel,[3] Dirk Poelman,[1,2] and Philippe F. Smet[1,2,‡]

[1]*LumiLab, Department of Solid State Sciences, Ghent University, 9000 Gent, Belgium*
[2]*Center for Nano- and Biophotonics (NB Photonics), Ghent University, 9000 Gent, Belgium*
[3]*European Synchrotron Radiation Facility (ESRF), 38000 Grenoble, France*

(Received 19 May 2020; accepted 23 June 2020; published 17 July 2020)

Laser excitation and x-ray spectroscopy are combined to settle a long-standing question in persistent luminescence. A reversible electron transfer is demonstrated, controlled by light and showing the same kinetics as the persistent luminescence. Exposure to violet light induces charging by oxidation of the excited Eu^{2+} while Dy^{3+} is simultaneously reduced. Oppositely, detrapping of Dy^{2+} occurs at ambient temperature or by infrared illumination, yielding afterglow or optically stimulated luminescence, respectively.

DOI: 10.1103/PhysRevLett.125.033001

Luminescent materials or phosphors are crucial for various technological applications, ranging from environmentally friendly lighting [1,2] to specialized applications in medicine and optoelectronics [3–7]. A subclass are those that feature energy storage capabilities, for which not all of the energy absorbed upon excitation is immediately emitted as photoluminescence. A fraction is used to transfer a charge carrier from the luminescent center to a so-called trap, generating a metastable state.

The lifetime of these metastable states can range over many orders of magnitude (quantified by the so-called trap depth). The long lifetimes of deep traps are exploited to date minerals or archeological artifacts, or for dosimeters, e.g., in medical imaging plates where red or infrared (IR) light is used to detrap charge carriers and induce the radiative decay of the luminescence activator, a process called optically stimulated luminescence (OSL) [8,9]. For luminescent materials with more shallow traps, ambient temperature can be sufficient to slowly deplete the traps (in minutes to hours), giving rise to the process of long afterglow or persistent luminescence [10–13]. This process can be accelerated by heating the phosphor, giving rise to thermoluminescence (TL), the analysis of which allows us to experimentally extract information on trap depths or trap depth distributions [14,15]. Afterglow materials hold the promise of new applications such as glow-in-the-dark traffic signalization [16], damage monitoring [17], radiation-free medical imaging [3,18], theranostics [19,20], cell characterization [21], or nanothermometry [22]. The storage capabilities need nevertheless to be improved in order to enable these advanced applications by the optimization of existing materials or the development of new ones [12,13].

In the 1990s it was found that some Eu^{2+} based phosphors acquire intense persistent luminescence upon codoping with a trivalent lanthanide ion (Ln^{3+}), often Dy^{3+} [23]. This triggered the discovery of a group of phosphors that can still be regarded as state of the art. Among them, the strontium aluminates ($SrAl_2O_4:Eu^{2+},Dy^{3+}$ and $Sr_4Al_{14}O_{25}:Eu^{2+},Dy^{3+}$) and the silicate $Sr_2MgSi_2O_7:Eu^{2+},Dy^{3+}$ take the most prominent places [10,12]. As the trapping capacity is significantly increased upon Dy^{3+} addition, it is tempting to identify the trivalent codopant as a trap. To date, no hard evidence has however been found that confirms or rejects a valence state change for Dy^{3+}. The reason for this standstill is the difficulty to detect such transient phenomenon in common structural and optical experiments, and the intrinsic complexity of these materials, making theoretical studies scarce and hard to correlate with experiments such as TL [24,25].

TL experiments have suggested that distributions of trap depths are present, rather than one discrete trap [15,26]. However, TL does not infer the chemical nature of the traps, and the distribution can be due to multiple intrinsic defects that induce trapping [27], but equally well to multiple nonequivalent Dy^{3+} centers in the crystal [28] distributed at different distances from the Eu^{2+} activator [29]. Detailed experimental studies of $SrAl_2O_4:Eu^{2+},Dy^{3+}$ suggest that trapping is local, i.e., close to the Eu^{2+} activator rather than a delocalization of the electron toward the conduction band [26]. A limited number of x-ray absorption spectroscopy studies have been reported on Eu^{2+}, Ln^{3+} codoped aluminates and silicates

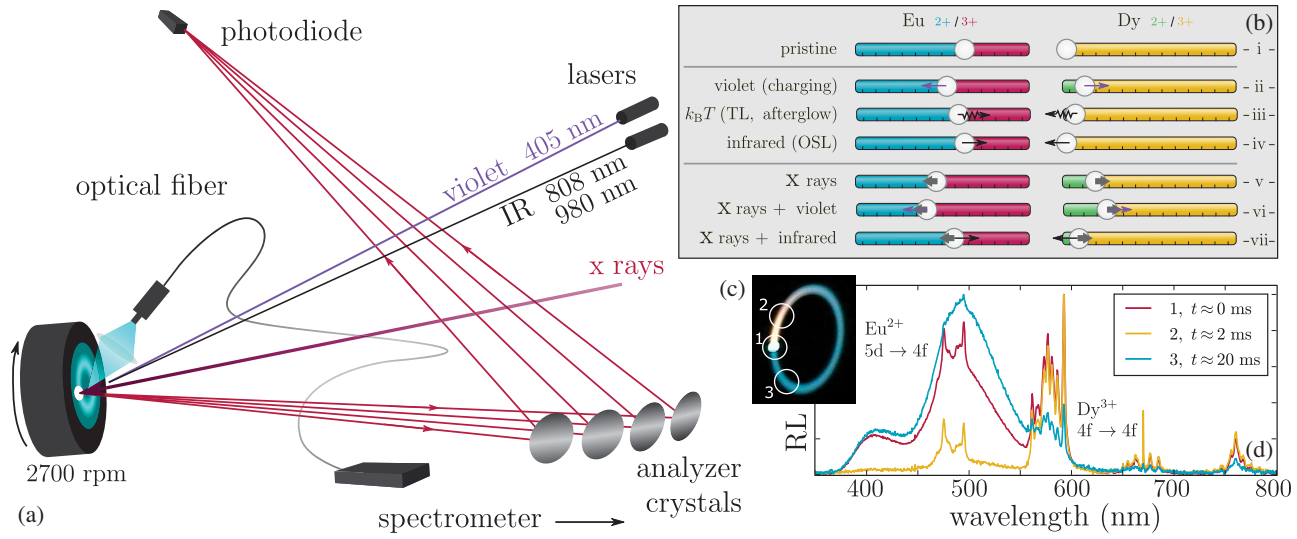

FIG. 1. Schematic representation of the experimental setup (a): monochromatic x rays strike the rotating sample, the x-ray fluorescence is analyzed by a spectrometer in Rowland geometry, using an array of spherically bent crystal analyzers and an avalanche photodiode. The sample is irradiated by violet or IR lasers and the radioluminescence (RL) is recorded. The schematic representation in (b) illustrates how light of different wavelengths, temperature, and x rays induce electron transfer and hence affect the Eu^{2+}-Eu^{3+} (blue-red) and Dy^{2+}-Dy^{3+} (green-yellow) equilibria in the phosphor. (c) Camera image of the rotating sample under steady-state conditions. The x-ray beam hits the sample at point 1. Normalized radioluminescence spectra are displayed (d), measured on three different spots on the rotating sample [indicated in (c)], featuring Eu^{2+} $4f^6 5d^1 \rightarrow 4f^7$ broadband (400–570 nm) and Dy^{3+} $4f^9 \rightarrow 4f^9$ line emissions at around 480, 575, 675, and 760 nm, following the $^4F_{9/2} \rightarrow {}^6H_J$ ($2J = 15, 13, 11, 9$) transitions, respectively.

[30–35]. Most studies failed to find reversible valence state changes, except for Korthout *et al.* who uncovered a partial oxidation of Eu^{2+} to Eu^{3+} in $SrAl_2O_4:Eu^{2+},Dy^{3+}$ [34]. Exposure to x rays does not only lead to radioluminescence (RL) from Eu^{2+} but also to charge trapping, as witnessed by the slow increase of RL intensity (the so-called charging) after switching on the x-ray beam and by the afterglow when switching off the x-ray beam. Traps were thermally cleaned to ensure that the electron transfer was reversible, i.e., that the observed oxidation was not due to a degradation process. This confirmed that indeed an electron is released from the Eu^{2+} ion during the charging (trapping) process, but no convincing information could be extracted on where it is trapped [34]. Carlson *et al.* recorded oxidation of Eu^{2+} in $Sr_2MgSi_2O_7:Eu$, but on a much longer timescale (hours) than the typical charging (seconds to minutes [26,34]), indicating that this was presumably caused by degradation, rather than the filling of traps [32].

Here, the valence state changes of Eu and Dy in $Sr_4Al_{14}O_{25}:Eu^{2+},Dy^{3+}$ persistent phosphors are recorded via resonant inelastic x-ray scattering (RIXS) [Fig. 1(a)]. It is found that a fraction of the Dy^{3+} is reduced to Dy^{2+} along with the oxidation of Eu^{2+} to Eu^{3+}, and that this reversible electron transfer is indeed responsible for the persistent luminescence.

The situation for a pristine Eu,Dy codoped persistent phosphor is represented in Fig. 1(b)(i), where Eu^{2+} and Eu^{3+} coexist with Dy^{3+}. Charging by blue to ultraviolet light [Fig. 1(b)(ii)] or x rays [Fig. 1(b)(v)] causes oxidation of a part of the Eu^{2+} while the redox partner, Dy^{3+} or another defect, gets reduced. This metastable state is long-lived and is slowly depleted at room temperature in the case of persistent phosphors [Fig. 1(b)(iii)], giving rise to afterglow or TL when the electron is transferred back to the Eu center. Infrared light has a similar effect by electronically exciting the trapped electron, giving rise to OSL [Fig. 1(b)(iv)].

X rays are ideal to probe the oxidation states of the dopants, but they simultaneously induce fast trapping, requiring measures to overcome this beam effect.

To slow down the x-ray induced charging, the sample was mounted on a rotating stage (spun at 2700 rpm), with the x-ray beam hitting 5 mm off axis. This allows us to probe a larger sample volume and reduces the number of photons per unit volume per unit time. Indeed, the time to reach a steady state (the equilibrium between the trapping effect of x rays and the detrapping processes) is hugely enlarged, passing from a few milliseconds to tens of seconds, enabling measurement of the time evolution of the x-ray induced charging.

In addition, the density of trapped charges can be controlled by illuminating the sample with violet or IR lasers (Fig. 1). This gives rise to the situations represented schematically in Figs. 1(b)(vi) and 1(b)(vii) where the effect of the lasers is superimposed on the effect of the x rays. The use of the external light sources hence allowed us to affect a fraction of the charges and create a differential effect on top of the unavoidable charging induced by x rays.

Finally, we could connect the x-ray measurements with the luminescence processes by collecting the RL emitted by the sample under x-ray irradiation. The parallel analysis of the two datasets was fundamental to ensure that the observations for Eu and Dy are indeed connected to the persistent luminescence process.

Our experiments were conducted on commercial $Sr_4Al_{14}O_{25}:Eu, Dy$ powders at beam line ID26 of the European Synchrotron Radiation Facility (ESRF) in Grenoble, France [36,37]. The sample was diluted in boron nitride, pressed to a pellet and mounted on a rotating sample stage. The Ln L_{III} absorption edges were used to probe the oxidation states of Eu and Dy. The rotating sample was positioned in the x-ray beam (Fig. 1). The incident photon energy was scanned across the Eu and Dy L_{III} edge. The maximum of the characteristic $L_{\alpha 1}$ emission was selected by an x-ray emission spectrometer based on Rowland geometry, resulting in high energy resolution fluorescence detected (HERFD) x-ray absorption near edge structure (XANES) spectra. Here, the main advantage of using the HERFD mode to collect XANES is its superior energy resolution which increments the sensitivity of the technique to small spectral variations [38–40]. Technical details are given in the Supplemental Material (SM) [41].

The spinning sample (16°/ms) allows us to record spectral changes upon continuous x-ray irradiation on a millisecond timescale [Figs. 1(c) and 1(d)]. The color of the luminescence changes, depending on the position, and hence on the time after irradiation [Fig. 1(d)]. This is analyzed in detail by recording the luminescence spectra at different positions (1, 2, 3) on the spinning pellet, corresponding to delays of 0, 2, and 20 ms after irradiation, respectively. Upon x-ray irradiation (position 1), different spectral components are clearly visible: the blue-green broadband $4f^6 5d^1 \rightarrow 4f^7$ emissions from Eu^{2+} in $Sr_4Al_{14}O_{25}$ peaking around 495 nm [42,43], as well as characteristic Dy^{3+} inter-$4f^9$ transitions, predominantly in the yellow. The first few milliseconds after irradiation (position 2), the parity and spin-allowed Eu^{2+} emission already decayed (order of 1 μs) and the slow-decaying Dy^{3+} emission dominates the spectrum. The Dy^{3+} decay is clearly visible on the picture in Fig. 1(c). After 20 ms (position 3), also the excited Dy^{3+} ions have largely decayed and the afterglow remains, showing a dominant Eu^{2+} $4f^6 5d^1 \rightarrow 4f^7$ emission. It is hence clear that the x rays are indeed able to induce the persistent luminescence.

Figure 2(a) shows HERFD XANES spectra, measured at the Eu L_{III} edge. These spectra feature two relatively sharp peaks, so-called white lines, that correspond to the resonant $2p^6 4f^N \rightarrow 2p^5 4f^N 5d^1$ electronic transition of Eu^{2+} ($N = 7$, around 6.975 keV) and Eu^{3+} ($N = 6$, around 6.983 keV) [44,45]. The characteristic 7–8 eV separation between Eu^{2+} and Eu^{3+} white lines, and more generally between Ln^{2+} and Ln^{3+} white lines [46,47], is often used to

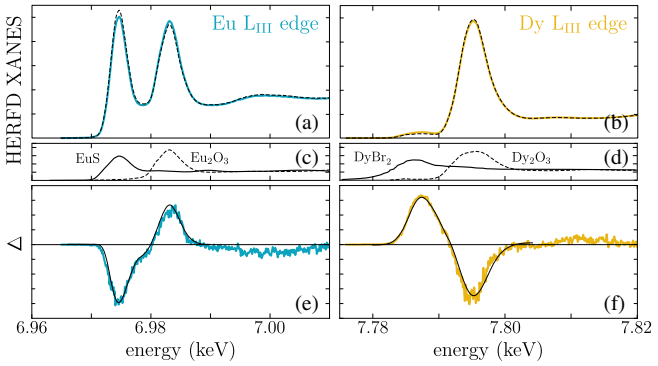

FIG. 2. High energy resolution fluorescence detected (HERFD) x-ray absorption near edge structure (XANES) spectra for the Eu (a) and Dy (b) L_{III} edges upon violet (colored line) or IR (black line) irradiation, compared to conventional XANES of reference spectra for (c) EuS (EuII) and Eu_2O_3 (EuIII) and (d) Dy_2O_3 (DyIII) and $DyBr_2$ (DyII, adapted from Ref. [46]), and the associated difference spectra Δ (colored lines) with their fit (black line) (e),(f).

acquire quantitative and qualitative information about the concurrence of lanthanide oxidation states [44,45].

It was previously found that Eu^{2+} oxidizes to Eu^{3+} in $SrAl_2O_4:Eu, Dy$ upon x-ray irradiation on the same timescale as the charging of the persistent luminescence [34]. Therefore, it is clear that the x rays, which are used as a probe for the lanthanide oxidation states, induce a net trapping effect, where a steady-state regime with a higher $[Eu^{3+}]:[Eu^{2+}]$ ratio, compared to a pristine sample, is established under irradiation [Fig. 1(b)(v)]. In order to push this dynamic equilibrium in both directions, laser stimulation was applied on top of the x-ray irradiation: violet light to further increase $[Eu^{3+}]:[Eu^{2+}]$ [Fig. 1(b)(vi)] and IR light to provoke detrapping, counteracting the effect of the x rays, thus lowering the $[Eu^{3+}]:[Eu^{2+}]$ ratio [Fig. 1(b)(vii)].

Figure 2 shows the effect of the laser stimulation. The blue curve, for violet stimulation, presents a higher $[Eu^{3+}]:[Eu^{2+}]$ ratio than the black curve, for IR stimulation. Interestingly, a similar but opposite effect was found for the same experiment, performed at the Dy L_{III} edge. The amount of Dy^{3+} goes slightly down upon violet stimulation (yellow curve), compared to IR stimulation (black curve). Concurrently, a small increase of the spectral intensity in the region where the Dy^{2+} white line is expected can be observed. Figures 2(e) and 2(f) display the differences between the HERFD XANES spectra, measured upon violet and IR stimulation, more clearly illustrating the valence changes.

The Dy^{2+} white line lies at lower energy than the Dy^{3+} white line, in the region where the Dy^{3+} preedge features are also observed [Fig. 2(d)]. The latter, which typically show a richer fine structure, are due to weakly allowed $2p^6 4f^9 \rightarrow 2p^5 4f^{10}$ transitions [48–51]. In our experiment, both features have a comparably low intensity. In order to

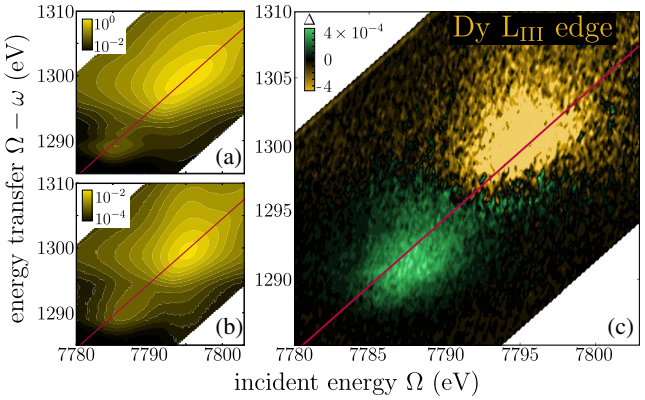

FIG. 3. RIXS planes of Dy_2O_3 (a) and $Sr_4Al_{14}O_{25}$:Eu, Dy (b), and the difference of RIXS planes of $Sr_4Al_{14}O_{25}$:Eu, Dy, measured upon violet and IR illumination (c). The red straight line corresponds to a scan of the incident energy at fixed emission energy (HERFD XANES). All planes measured at the Dy L_{III} edge.

confirm that the changes below the Dy^{3+} white line are indeed due to the creation of Dy^{2+}, RIXS planes (see SM [41]) were measured under both violet and IR illumination and compared to RIXS planes of the preedge region (Fig. 3). The Dy^{3+} preedge structure is clearly seen in the RIXS plane of Dy_2O_3 in the range of $\Omega = 7785$ eV, but it is broadened for the phosphor sample. The difference of the violet and IR illuminated RIXS planes confirms that the spectral changes correspond to a decrease of the amount of Dy^{3+} and an increase of Dy^{2+}: two broad bands are found, consistent with the rise of a Dy^{2+} white line, rather than with changes in the Dy^{3+} preedge region. This explains why the Dy^{3+} preedge structure is obscured for the phosphor sample as the x rays inevitably create some Dy^{2+} in the phosphor [see also Fig. 1(b)].

These observations clearly prove the existence of the following photoinduced electron transfer,

$$Eu^{2+} + Dy^{3+} \underset{k_BT}{\overset{\text{violet}}{\underset{\text{IR}}{\overset{\text{x rays}}{\rightleftharpoons}}}} Eu^{3+} + Dy^{2+}, \qquad (1)$$

in accordance with the scheme in Fig 1(b). To obtain reliable estimates for the quantity of Eu and Dy that changes oxidation states, the HERFD XANES spectra were fitted [52–55] with two Gaussians, one for each white line, and a smooth step function, representing the electronic transitions toward the dense set of unbound states, $2p^6 4f^N \rightarrow 2p^5 4f^N \phi^1$ (see also SM [41]). The result for the difference spectra is shown in Figs. 2(e) and 2(f).

The area under the white line is associated with the concentration of Ln ions [44–46]. By exploiting that the total number of Ln ions remains constant throughout the experiment, it was verified that difference spectra of Figs. 2(e) and 2(f) correspond to 3% of all Eu and 2% of all Dy. Given the higher concentration of Dy in the

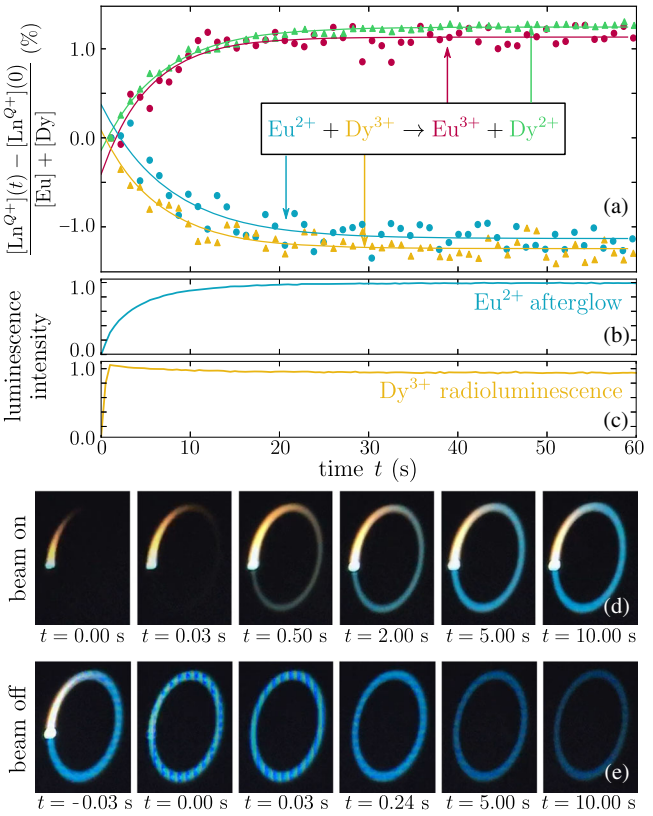

FIG. 4. Time evolution of the lanthanide oxidation states, relative to the total [Eu] + [Dy] content from HERFD XANES (a). The x-ray beam is switched on at time $t = 0$. Simultaneously, the luminescence is probed for Eu^{2+} (broadband emission in 450–550 nm range) (b) and Dy^{3+} (line emission in 550–600 nm range) (c). Camera images of a pristine rotating sample illustrate the charging and persistent luminescence of the blue Eu^{2+} emission when the beam is switched on (d) and off (e), respectively.

phosphor (as verified by energy-dispersive x-ray spectroscopy [56]; see SM [41]), quantitative agreement is found between the valence changes of Eu and Dy within the experimental uncertainties. This number is of the same order of magnitude as a prior estimate for the number of Eu ions changing valence state, based on optical spectroscopy experiments on $SrAl_2O_4$:Eu, Dy [57].

The connection between the electron transfer and the persistent luminescence is substantiated by measuring their time evolution (Fig. 4). An optically cleaned phosphor, i.e., for which all traps were first emptied by OSL, is irradiated by the x-ray beam from $t = 0$. The oxidation states of the lanthanide ions are sampled every second by recording the maximum of the white line for every oxidation state separately (see SM [41]). Figure 4(a) shows that the x-ray induced oxidation of Eu^{2+} and reduction of Dy^{3+} occur on the same timescale of about 20 s. After this, a dynamic equilibrium is reached where the forward and backward electron transfers, Eq. (1), occur at the same rate. This relatively long timescale is the consequence of the sample being mounted on a rotating stage, uniformly probing a

sample area which is ≈280 times larger than for a static sample (with a rotation period of ≈22 ms, each measured point is averaged over several rotations). For a static sample, the dynamic equilibrium would have been reached after 0.1 s, presumably explaining why no valence state changes were found in prior investigations [30–33,35].

The charging of the persistent luminescence, monitored by the increasing Eu^{2+} emission, follows indeed the same temporal behavior as the electron transfer [Fig. 4(b)]. In the same time frame of the charging, the Dy^{3+} RL intensity shows a small decrease, presumably due to the partial reduction of the Dy^{3+} ions [Eq. (1)].

The variations in luminescence are also visible in Fig. 4(d), showing the rotating sample at several time delays after switching on the x-ray beam. The comma-shaped signature of the Dy^{3+} RL appears instantaneously, while the blue persistent luminescence builds up more slowly (see SM [41] for the associated intensity profiles [58,59]). Complementarily, the Dy^{3+} RL disappears almost immediately after switching off the x-ray beam [Fig. 4(e)], leaving the blue afterglow visible for several hours. The first two frames confirm that the intensity of the blue Eu^{2+} luminescence that is probed during this experiment is due solely to the afterglow; i.e., the blue intensity along the race track does not change abruptly when the excitation is switched off.

In summary, a dedicated RIXS study is performed on $Sr_4Al_{14}O_{25}:Eu,Dy$ persistent luminescent materials in order to elucidate the electron transfer that underlies the energy storage process. While the x rays allow us to accurately probe the oxidation states of both dopants in real time, they unavoidably disturb the equilibrium electron occupation, prohibiting the unambiguous assessment of the persistent luminescence mechanism unless measures are taken to overcome the beam effect. A novel measurement approach is demonstrated, where illumination with visible and near-IR light are used to manipulate the electron occupations, in combination with an effective method to spread the applied x-ray dose by rapidly spinning the sample. Excitation by violet light induces trapping, creating metastable Eu^{3+}-Dy^{2+} centers, while IR light provokes detrapping. Quantitatively, 3% of the Eu ions and a corresponding number of Dy ions are affected, in agreement with the optically determined storage capacity. The characteristic time of the metastable Eu^{3+}-Dy^{2+} state coincides with the charging of the persistent luminescence. This is hence the first confirmation of the popular, yet debated, model where Dy^{3+} acts as the main electron trap in persistent phosphors.

J. J. J. and P. F. S. acknowledge the Ghent University Special Research Fund via the projects BOF/PDO/2017/002101 and GOA-Enclose, respectively. We acknowledge the European Synchrotron Radiation Facility (ESRF) for the allocation of beamtime (beamline ID26).

*jonas.joos@UGent.be
†Present address: Helmholtz-Zentrum Dresden-Rossendorf, 01314 Dresden, Germany.
‡philippe.smet@UGent.be

[1] J. W. Qiao, M. Amachraa, M. Molokeev, Y. C. Chuang, S. P. Ong, Q. Y. Zhang, and Z. G. Xia, Engineering of $K_3YSi_2O_7$ to tune photoluminescence with selected activators and site occupancy, Chem. Mater. **31**, 7770 (2019).
[2] J. Qiao, G. Zhou, Y. Zhou, Q. Zhang, and Z. Xia, Divalent europium-doped near-infrared-emitting phosphor for light-emitting diodes, Nat. Commun. **10**, 5267 (2019).
[3] T. Maldiney, A. Bessiere, J. Seguin, E. Teston, S. K. Sharma, B. Viana, A. J. J. Bos, P. Dorenbos, M. Bessodes, D. Gourier, D. Scherman, and C. Richard, The *in vivo* activation of persistent nanophosphors for optical imaging of vascularization, tumours and grafted cells, Nat. Mater. **13**, 418 (2014).
[4] D. Hayashi, A. M. van Dongen, J. Boerekamp, S. Spoor, G. Lucassen, and J. Schleipen, A broadband LED source in visible to short-wave-infrared wavelengths for spectral tumor diagnostics, Appl. Phys. Lett. **110**, 233701 (2017).
[5] V. Rajendran, M. H. Fang, G. N. De Guzman, T. Lesniewski, S. Mahlik, M. Grinberg, G. Leniec, S. M. Kaczmarek, Y. S. Lin, K. M. Lu, C. M. Lin, H. Chang, S. F. Hu, and R. S. Liu, Super broadband near-infrared phosphors with high radiant flux as future light sources for spectroscopy applications, ACS Energy Lett. **3**, 2679 (2018).
[6] E. Song, X. Jiang, Y. Zhou, Z. Lin, S. Ye, Z. Xia, and Q. Zhang, Heavy Mn^{2+} doped $MgAl_2O_4$ phosphor for high-efficient near-infrared light-emitting diode and the night-vision application, Adv. Opt. Mater. **7**, 1901105 (2019).
[7] L. Zhang, D. Wang, Z. Hao, X. Zhang, G. Pan, H. Wu, and J. Zhang, Cr^{3+}-doped broadband NIR garnet phosphor with enhanced luminescence and its application in NIR spectroscopy, Adv. Opt. Mater. **7**, 1900185 (2019).
[8] P. A. Jursinic, Characterization of optically stimulated luminescent dosimeters, OSLDs, for clinical dosimetric measurements, Med. Phys. **34**, 4594 (2007).
[9] E. G. Yukihara and S. W. S. McKeever, Optically stimulated luminescence (OSL) dosimetry in medicine, Phys. Med. Biol. **53**, R351 (2008).
[10] K. Van den Eeckhout, P. F. Smet, and D. Poelman, Persistent luminescence in Eu^{2+}-doped compounds: A review, Materials **3**, 2536 (2010).
[11] Y. Li, M. Gecevicius, and J. Qiu, Long persistent phosphors—From fundamentals to applications, Chem. Soc. Rev. **45**, 2090 (2016).
[12] R. E. Rojas-Hernandez, F. Rubio-Marcos, M. Á. Rodriguez, and F. Fernandez, Long lasting phosphors: $SrAl_2O_4:Eu,Dy$ as the most studied material, Renew. Sustain. Energ. Rev. **81**, 2759 (2018).
[13] J. Xu and S. Tanabe, Persistent luminescence instead of phosphorescence: History, mechanism, and perspective, J. Lumin. **205**, 581 (2019).
[14] A. J. J. Bos, Theory of thermoluminescence, Radiation Measurements **41**, S45 (2006).

[15] K. Van den Eeckhout, A. J. J. Bos, D. Poelman, and P. F. Smet, Revealing trap depth distributions in persistent phosphors, Phys. Rev. B **87**, 045126 (2013).

[16] J. Botterman and P. F. Smet, Persistent phosphor $SrAl_2O_4:Eu,Dy$ in outdoor conditions: Saved by the trap distribution, Opt. Express **23**, A868 (2015).

[17] R. R. Petit, S. E. Michels, A. Feng, and P. F. Smet, Adding memory to pressure-sensitive phosphors, Light Sci. Appl. **8**, 124 (2019).

[18] H. Terraschke, M. Franzreb, and C. Wickleder, Magnetism and afterglow united: Synthesis of novel double core-shell Eu^{2+}-doped bifunctional nanoparticles, Chem. Eur. J. **26**, 6833 (2020).

[19] T. Lécuyer, E. Teston, G. Ramirez-Garcia, T. Maldiney, B. Viana, J. Seguin, N. Mignet, D. Scherman, and C. Richard, Chemically engineered persistent luminescence nanoprobes for bioimaging, Theranostics **6**, 2488 (2016).

[20] L. Yan, L. Chen, X. Zhao, and X. Yan, pH switchable nanoplatform for *in vivo* persistent luminescence imaging and precise photothermal therapy of bacterial infection, Adv. Funct. Mater. **30**, 1909042 (2020).

[21] A. Harizaj, O. Q. De Clercq, B. Descamps, C. Vanhove, S. C. De Smedt, D. Poelman, I. Lentacker, and K. Braeckmans, Biocompatible lipid-coated persistent luminescent nanoparticles for *in vivo* imaging of dendritic cell migration, Part. Part. Syst. Charact. **36**, 1900371 (2019).

[22] E. M. Rodríguez, G. López-Peña, E. Montes, G. Lifante, J. G. Solé, D. Jaque, L. A. Diaz-Torres, and P. Salas, Persistent luminescence nanothermometers, Appl. Phys. Lett. **111**, 081901 (2017).

[23] T. Matsuzawa, Y. Aoki, N. Takeuchi, and Y. Murayama, New long phosphorescent phosphor with high brightness, $SrAl_2O_4:Eu^{2+},Dy^{3+}$, J. Electrochem. Soc. **143**, 2670 (1996).

[24] J. Cai, W. Jing, J. Cheng, Y. Zhang, Y. Chen, M. Yin, Y. Y. Yeung, and C. K. Duan, First-principles calculations of photoluminescence and defect states of Ce^{3+}-doped $(Ca/Sr)_2B_5O_9Cl$, Phys. Rev. B **99**, 125107 (2019).

[25] Micah P. Prange, Niranjan Govind, and Sebastien N. Kerisit, *Ab initio* calculations of the rate of carrier trapping and release at dopant sites in NaI:Tl beyond the harmonic approximation, Phys. Rev. B **101**, 024304 (2020).

[26] J. Botterman, J. J. Joos, and P. F. Smet, Trapping and detrapping in $SrAl_2O_4:Eu,Dy$ persistent phosphors: Influence of excitation wavelength and temperature, Phys. Rev. B **90**, 085147 (2014).

[27] V. Laguta, M. Buryi, P. Arhipov, O. Sidletskiy, O. Laguta, M. G. Brik, and M. Nikl, Oxygen-vacancy donor-electron center in $Y_3Al_5O_{12}$ garnet crystals: Electron paramagnetic resonance and dielectric spectroscopy study, Phys. Rev. B **101**, 024106 (2020).

[28] T. Delgado, S. Ajoubipour, J. Afshani, S. Yoon, B. Walfort, and H. Hagemann, Spectroscopic properties of Dy^{3+}- and Dy^{3+}, B^{3+}- doped $SrAl_2O_4$, Opt. Mater. **89**, 268 (2019).

[29] C. MacKeen, F. Bridges, L. Seijo, Z. Barandiarán, M. Kozina, A. Mehta, M. F. Reid, and J. P. R. Wells, The complexity of the $CaF_2:Yb$ system: A huge, reversible, x-ray-induced valence reduction, J. Phys. Chem. C **121**, 28435 (2017).

[30] Z. Qi, C. Shi, M. Liu, D. Zhou, X. Luo, J. Zhang, and Y. Xie, The valence of rare earth ions in $R_2MgSi_2O_7:Eu,Dy$ (R = Ca, Sr) long-afterglow phosphors, Phys. Status Solidi A **201**, 3109 (2004).

[31] T. Aitasalo, J. Hassinen, J. Hölsä, T. Laamanen, M. Lastusaari, Malkamäki, J. Niittykoski, and P. Novák, Synchrotron radiation investigations of the $Sr_2MgSi_2O_7:Eu^{2+},R^{3+}$ persistent luminescence materials, J. Rare Earth **27**, 529 (2009).

[32] S. Carlson, J. Hölsä, T. Laamanen, M. Lastusaari, M. Malkamaki, J. Niittykoski, and R. Valtonen, X-ray absorption study of rare earth ions in $Sr_2MgSi_2O_7:Eu^{2+},R^{3+}$ persistent luminescence materials, Opt. Mater. **31**, 1877 (2009).

[33] J. Hölsä, T. Laamanen, M. Lastusaari, M. Malkamäki, E. Welter, and D. A. Zajac, Valence and environment of rare earth ions in $CaAl_2O_4:Eu^{2+},R^{3+}$ persistent luminescence materials, Spectrochim. Acta B Atom. Spectros. **65**, 301 (2010).

[34] K. Korthout, K. Van den Eeckhout, J. Botterman, S. Nikitenko, D. Poelman, and P. F. Smet, Luminescence and x-ray absorption measurements of persistent $SrAl_2O_4:Eu,Dy$ powders: Evidence for valence state changes, Phys. Rev. B **84**, 085140 (2011).

[35] M. Lastusaari, H. F. Brito, S. Carlson, J. Hölsä, T. Laamanen, L. C. V. Rodrigues, and E. Welter, Valences of dopants in Eu^{2+} persistent luminescence materials, Phys. Scr. **89**, 044004 (2014).

[36] C. Gauthier, V. A. Sole, R. Signorato, J. Goulon, and E. Moguiline, The ESRF beamline ID26: X-ray absorption on ultra dilute sample, J. Synchrotron Radiat. **6**, 164 (1999).

[37] P. Glatzel, T. C. Weng, K. Kvashnina, J. Swarbrick, M. Sikora, E. Gallo, N. Smolentsev, and R. A. Mori, Reflections on hard x-ray photon-in/photon-out spectroscopy for electronic structure studies, J. Electron Spectrosc. Relat. Phenom. **188**, 17 (2013).

[38] K. Hämäläinen, D. P. Siddons, J. B. Hastings, and L. E. Berman, Elimination of the Inner-Shell Lifetime Broadening in X-Ray-Absorption Spectroscopy, Phys. Rev. Lett. **67**, 2850 (1991).

[39] P. Carra, M. Fabrizio, and B. T. Thole, High Resolution X-Ray Resonant Raman Scattering, Phys. Rev. Lett. **74**, 3700 (1995).

[40] P. Glatzel and U. Bergmann, High resolution 1s core hole x-ray spectroscopy in 3d transition metal complexes—Electronic and structural information, Coord. Chem. Rev. **249**, 65 (2005).

[41] See Supplemental Material at http://link.aps.org/supplemental/10.1103/PhysRevLett.125.033001 for additional information on the experimental methods and fitting of HERFD XANES spectra.

[42] D. Dutczak, C. Ronda, T. Jüstel, and A. Meijerink, Anomalous trapped exciton and d-f emission in $Sr_4Al_{14}O_{25}:Eu^{2+}$, J. Phys. Chem. A **118**, 1617 (2014).

[43] D. Dutczak, T. Jüstel, C. Ronda, and A. Meijerink, Eu^{2+} luminescence in strontium aluminates, Phys. Chem. Chem. Phys. **17**, 15236 (2015).

[44] M. E. Fieser, M. G. Ferrier, J. Su, E. Batista, S. K. Cary, J. W. Engle, W. J. Evans, J. S. Lezama Pacheco, S. A.

Kozimor, A. C. Olson, A. J. Ryan, B. W. Stein, G. L. Wagner, D. H. Woen, T. Vitova, and P. Yang, Evaluating the electronic structure of formal Ln^{II} ions in $Ln^{II}(C_5H_4SiMe_3)_3^{1-}$ using XANES spectroscopy and DFT calculations, Chem. Sci. **8**, 6076 (2017).

[45] L. Amidani, K. Korthout, J. J. Joos, M. van der Linden, H. F. Sijbom, A. Meijerink, D. Poelman, P. F. Smet, and P. Glatzel, Oxidation and luminescence quenching of europium in $BaMgAl_{10}O_{17}$ blue phosphors, Chem. Mater. **29**, 10122 (2017).

[46] Z. Hu, G. Kaindll, and G. Meyer, X-ray absorption near-edge structure at the L_{I-III} thresholds of Pr, Nd, Sm, and Dy compounds with unusual valences, J. Alloys Compd. **246**, 186 (1997).

[47] J. F. Herbst and J. W. Wilkins, Relativistic calculations of $2p$ excitation energies in the rare-earth metals, Phys. Rev. B **26**, 1689 (1982).

[48] A. V. Soldatov, T. S. Ivanchenko, S. Della Longa, A. Kotani, Y. Iwamoto, and A. Bianconi, Crystal-structure effects in the Ce L_3-edge x-ray-absorption spectrum of CeO_2: Multiple-scattering resonances and many-body final states, Phys. Rev. B **50**, 5074 (1994).

[49] S. Tanaka, K. Okada, and A. Kotani, Resonant x-ray emission spectroscopy in Dy compounds, J. Phys. Soc. Jpn. **63**, 2780 (1994).

[50] F. Bartolomé, J. M. Tonnerre, L. Sève, D. Raoux, J. Chaboy, L. M. García, M. Krisch, and C. C. Kao, Identification of Quadrupolar Excitation Channels at the L_3 Edge of Rare-Earth Compounds, Phys. Rev. Lett. **79**, 3775 (1997).

[51] M. Nakazawa, K. Fukui, H. Ogasawara, A. Kotani, and C. F. Hague, X-ray absorption and resonant x-ray emission spectra by electric quadrupole excitation in light rare-earth systems, Phys. Rev. B **66**, 113104 (2002).

[52] J. Prietzel, A. Botzaki, N. Tyufekchieva, M. Brettholle, J. Thieme, and W. Klysubun, Sulfur speciation in soil by S K-edge XANES spectroscopy: Comparison of spectral deconvolution and linear combination fitting, Environ. Sci. Technol. **45**, 2878 (2011).

[53] G. S. Henderson, F. M. F. de Groot, and B. J. A. Moulton, X-ray absorption near-edge structure (XANES) spectroscopy, Rev. Mineral. Geochem. **78**, 75 (2014).

[54] G. Bunker, *Introduction to XAFS: A Practical Guide to X-Ray Absorption Fine Structure Spectroscopy* (Cambridge University Press, New York, 2010).

[55] J. A. van Bokhoven and C. Lamberti, *X-Ray Absorption and X-Ray Emission Spectroscopy: Theory and Applications*, Vol. 1 (Wiley, Chichester, 2016).

[56] R. H. Packwood and J. D. Brown, A Gaussian expression to describe $\phi(\rho z)$ curves for quantitative electron probe microanalysis, X-Ray Spectrom. **10**, 138 (1981).

[57] D. Van der Heggen, J. J. Joos, D. C. R. Burbano, J. A. Capobianco, and P. F. Smet, Counting the photons: Determining the absolute storage capacity of persistent phosphors, Materials **10**, 867 (2017).

[58] C. A. Schneider, W. S. Rasband, and K. W. Eliceiri, NIH image to ImageJ: 25 years of image analysis, Nat. Methods **9**, 671 (2012).

[59] C. T. Rueden, J. Schindelin, M. C. Hiner, B. E. DeZonia, A. E. Walter, E. T. Arena, and K. W. Eliceiri, ImageJ2: ImageJ for the next generation of scientific image data, BMC Bioinf. **18**, 529 (2017).